

An unbiased statistical study of the metallicity of core-collapse supernovae based on VLT/MUSE integral-field-unit spectroscopy

Qiang Xi^{1,2} Ning-Chen Sun^{1,2,3}★ Yi-Han Zhao^{1,2} Justyn R. Maund⁴ Zexi Niu^{1,2}

Adam J. Singleton⁵ Jifeng Liu^{1,2,3,6}

¹*School of Astronomy and Space Science, University of Chinese Academy of Sciences, Beijing 100049, People's Republic of China*

²*National Astronomical Observatories, Chinese Academy of Sciences, Beijing 100101, People's Republic of China*

³*Institute for Frontiers in Astronomy and Astrophysics, Beijing Normal University, Beijing, 102206, People's Republic of China*

⁴*Department of Physics, Royal Holloway, University of London, Egham, TW20 0EX, United Kingdom*

⁵*School of Mathematical and Physical Sciences, University of Sheffield, Hicks Building, Hounsfield Road, Sheffield S3 7RH, United Kingdom*

⁶*New Cornerstone Science Laboratory, National Astronomical Observatories, Chinese Academy of Sciences, Beijing 100012, People's Republic of China*

Accepted XXX. Received YYY; in original form ZZZ

ABSTRACT

Metallicity plays a crucial role in the evolution of massive stars and their final core-collapse supernova (CCSN) explosions. Integral-field-unit (IFU) spectroscopy can provide a spatially resolved view of SN host galaxies and serve as a powerful tool to study SN metallicities. Early transient surveys targeted bright galaxies with high star formation and SN rates; as a result, the discovered SNe are significantly biased toward high metallicities. More recently, the untargeted, wide-field transient surveys, such as ASAS-SN and ZTF, have discovered a large number of SNe without such a bias. In this work, we construct a large and unbiased sample of SNe discovered by (quasi-) untargeted searches, consisting of 209 SNe of Types II (with unknown subtypes), IIP, IIn, IIb, Ib and Ic at $z \leq 0.02$ with VLT/MUSE observations. This is currently the largest CCSN sample with IFU observations. With the strong-line method, we reveal the spatially-resolved metallicity maps of the SN host galaxies and acquire accurate metallicity measurements for the SN sites. Our results show that the SN metallicities range from $12 + \log(\text{O}/\text{H}) = 8.1$ to 8.7 dex, and the metallicity distributions for different SN types are very close to each other, with mean and median values of 8.4–8.5 dex. We carefully analysed the stochastic sampling effect, showing that our large sample size narrows the 1σ uncertainty down to only 0.05 dex. The apparent metallicity differences among SN types are all within 3σ uncertainties and the metallicity distributions for different SN types are all consistent with being randomly drawn from the same reference distribution. This suggests that metallicity plays a minor role in the origin of different CCSN types and some other metallicity-insensitive processes, such as binary interaction, dominate the distinction of CCSN types.

Key words: SNe: general – star: mass-loss

1 INTRODUCTION

Supernovae (SNe) are one of the most energetic catastrophic events in the Universe. They are categorized into Type I and Type II based on the presence of hydrogen lines in their spectra (Filippenko 1997). Other than the thermonuclear Type Ia SNe, the other types originate from the core collapse (CC) of massive stars with initial masses of $\geq 8 M_{\odot}$ (Bethe et al. 1979; Woosley & Weaver 1986; Arnett et al. 1989). Most hydrogen-rich SNe are of Type IIP, characterised by a plateau phase, powered by hydrogen recombination, in the light curve. A fraction of SNe, classified as Type IIn, exhibit narrow emission lines in their spectra arising from the strong interaction between the fast SN ejecta and slow circumstellar material (CSM; Kiewe et al. 2012). Type Ib and Type Ic SNe are characterized by the absence of hydrogen features in their spectra, with Type Ic SNe also lacking helium features (Filippenko 1997). As an intermediate class between the hydrogen-rich and hydrogen-poor SNe, Type IIb displays hydro-

gen lines in the early phases of the explosion, resembling Type II, but these features disappear quickly in the later stages, appearing similar to Type Ib (Nomoto et al. 1993). For Types IIb, Ib and Ic, the disappearance or lack of hydrogen/helium features are due to the stripping of the outer envelopes of their progenitor stars. They are also known, therefore, as the stripped-envelope (SE) SNe.

It is a major goal, and currently a major difficulty, to determine the progenitor stars of different types of SNe. Current research suggests that the progenitors of Type IIP SNe are red supergiants (RSGs) with massive hydrogen envelopes (Smartt 2009; Niu et al. 2023; Hong et al. 2024). However, stellar evolutionary theories are inconsistent with the lack of detection of high-mass (>16 – $18 M_{\odot}$) RSG progenitors (i.e. the "RSG problem"; Smartt 2009). This could result from CSM extinction underestimating the progenitor RSG's mass (Beasor et al. 2024) or from high-mass RSGs collapsing directly into black holes without a supernova (Kochanek 2014). It is also unclear whether Type IIP SNe could come from interacting binary systems (Zapartas et al. 2021; Bostroem et al. 2023, Niu et al. in preparation). While luminous blue variables (LBVs) have been proposed as

★ E-mail: sunnc@ucas.ac.cn

Type II_n SN progenitors (Smith 2014; Niu et al. 2024a), it is still unclear why these stars undergo intense outbursts, creating the dense CSM, shortly before explosion. SESNe could originate from single massive WR stars (Woosley & Weaver 1986), stripped by wind, or binary systems, where the progenitor is stripped by a companion star (Podsiadlowski et al. 1992; Sun et al. 2020a,b, 2021, 2022, 2023; Niu et al. 2024b; Zhao et al. 2024). It still remains an open question what fraction of SESNe each channel contributes to.

Metallicity plays a crucial role in the evolution of massive stars. At high metallicities, stars have stronger line-driven winds, allowing for the stripping of the envelope and the formation of CSM (Castor et al. 1975). These effects can determine the light curve and spectral features, and even the classification, of their final SN explosion. Environmental studies offer a powerful approach to investigate the metallicity of CCSNe. During the short lifetimes ($\lesssim 50$ million years) of massive stars, they can travel only a short distance from the formation to explosion sites and the environment has limited chemical evolution over such short timescales (Anderson et al. 2015).

Early studies on SN metallicity relied on long-slit spectroscopy (Anderson et al. 2010; Modjaz et al. 2011; Leloudas et al. 2011; Sanders et al. 2012; Taddia et al. 2015) or even used the metallicity of the entire host galaxy as a proxy (Langer & Norman 2006; Prieto et al. 2008; Neill et al. 2011; Lunnan et al. 2014). It has been suggested, however, that a high spatial resolution is necessary for the accurate measurement of SN metallicity based on gas emission lines from the environment (Niino et al. 2015). In more recent years, integral-field-unit (IFU) spectroscopy has been used to investigate SN metallicity (Kuncarayakti et al. 2012a, 2013a,b, 2015, 2018; Galbany et al. 2014, 2016, 2018; Pessi et al. 2023; Moriya et al. 2023). Instead of a single point or slit, IFU has the capability of acquiring spatially resolved spectral information over a significant portion of sky. This is important to reveal the complexity of the SN environment. A generally increasing trend in metallicity has been suggested for IIP \rightarrow IIb \rightarrow Ib \rightarrow Ic, correlated with the degree of envelope stripping.

In statistical studies, an unbiased sample is very important. Limited by the telescopes' small field of view, early SN searches targeted on galaxies of high masses and star formation rates (SFRs) in order to maximize the number of discovered SNe. Such galaxies, however, also tend to have higher metallicities (Tremonti et al. 2004), thus introducing a bias to SN samples discovered in this way (Sanders et al. 2012). With the increasing power of time-domain observations, more recent SN searches are able to observe a large number of, almost randomly selected, galaxies (e.g. the Lick Observatory Supernova Search (LOSS; Filippenko et al. 2001) or even map a significant portion of sky (e.g. the All Sky Automated Survey for SNe (ASAS-SN; Kochanek et al. 2017)). SNe discovered by such untargeted or quasi-untargeted searches are not affected by the metallicity bias introduced by their host galaxies. Figure 1 compares the host galaxy magnitudes of CCSNe discovered before 2010, when most were discovered by targeted searches, and after 2016, when most were discovered by (quasi-) untargeted searches. It is clear that SNe from targeted searches are significantly biased toward brighter host galaxies. Therefore, the early studies on SN metallicity are unavoidably affected by the bias caused by targeted SN discovery.

For studies that rely on archival observations, another potential bias may come from data availability as the archival observations are from different programs with different scientific goals, target selection criteria, observational strategies and even telescopes. Without a further careful selection, the sample could be rather heterogeneous with significant biases that are difficult to assess.

A large sample size is also very important to reduce the stochastic sampling effect. In this work, we study SN metallicity based on IFU

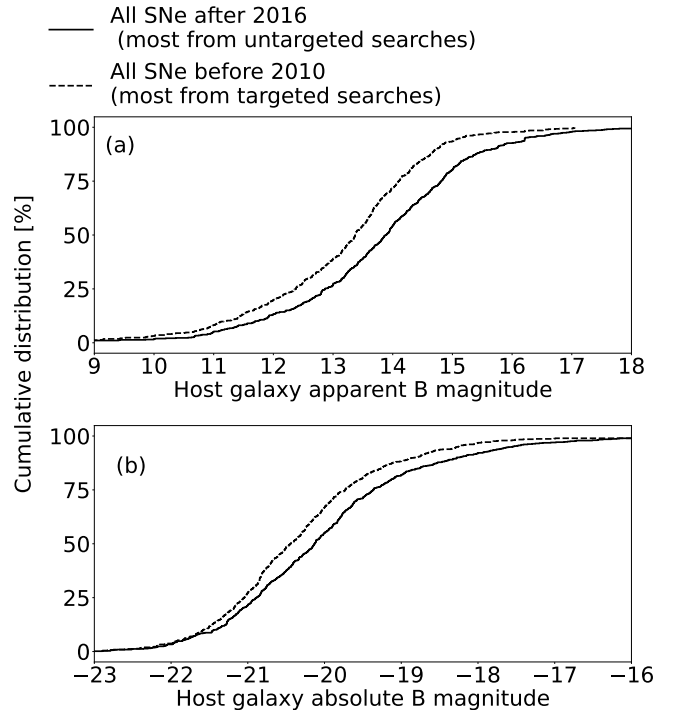


Figure 1. Cumulative distributions of the apparent (a) and absolute (b) B-band magnitudes of SN host galaxies. The dashed line is for SNe before 2010, when most were discovered by transient surveys targeted on bright galaxies, while the solid line is for those after 2016, when most were discovered by untargeted SN searches. Magnitudes for SN host galaxies are from the GLADE+ catalog (Dálya et al. 2018).

observations carried out by the Multi-Unit Spectroscopic Explorer (MUSE) on the Very Large Telescope (VLT). With a careful selection, we build a large and unbiased sample of 209 CCSNe, which is to date the largest SN sample with IFU data. We try to look for metallicity difference among the SN types. Our aim is to explore the possible roles played by metallicity in the origin of CCSNe.

This paper is organized as follows: Section 2 explains our sample selection and metallicity measurement. Section 3 presents our results along with a discussion of key implications. Finally, this work is summarized in Section 4.

2 METHOD

2.1 Sample selection

MUSE is an IFU instrument installed on the VLT operated by the European Southern Observatory (ESO) in Chile. It has a large field of view of 1×1 arcmin² and covers a wavelength range from 4650 to 9300 Å (Bacon et al. 2010). This range covers the important gas emission lines (such as H α , H β , [O III] $\lambda\lambda$ 4959, 5007, and [N II] $\lambda\lambda$ 6548, 6583), with which metallicity can be derived with the strong-line method (Pagel et al. 1979; Edmunds & Pagel 1984). MUSE is, therefore very suitable for SN metallicity studies.

We cross-match the MUSE-Wide survey data in ESO Data Archive¹ to the Transient Name Server² (TNS) and Open SN Catalog

¹ <https://archive.eso.org/scienceportal/home>

² <https://www.wis-tns.org/>

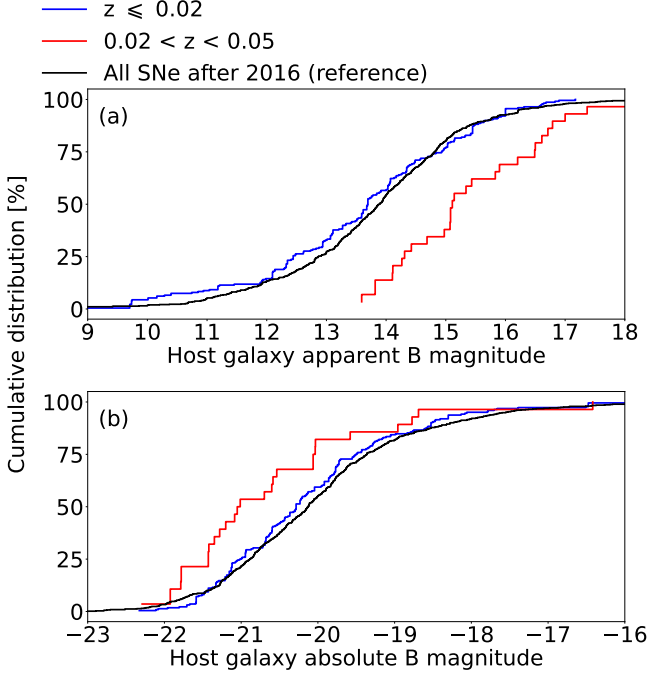


Figure 2. Cumulative distributions of the apparent (a) and absolute (b) B-band magnitudes of SN host galaxies. The black line is for all SNe after 2016, when most were discovered by untargeted SN searches (same as the black solid line in Fig. 1). They suffer little from discovery bias and are used as a reference distribution. The blue and red lines are SNe discovered by (quasi-) untargeted searches and with MUSE observations at redshift of $z \leq 0.02$ and $0.02 < z < 0.05$, respectively.

(OSC; Guillochon et al. 2017), finding host galaxies of 465 CCSNe with MUSE data at a redshift $z < 0.05$. As mentioned in the Introduction, further careful selection is crucial to construct an unbiased sample for the statistical analysis of SN metallicities. The two key considerations are SN discovery and data availability.

SN discovery We include in our sample SNe discovered in two ways. (1) SNe discovered by the untargeted, wide-field transient surveys, including the (Intermediate) Palomar Transient Factory (PTF; Law et al. 2009; Cao et al. 2016), ZTF (Bellm et al. 2019), ASAS-SN (Kochanek et al. 2017), Pan-STARRS (Chambers et al. 2019), the Australia Telescope Large Area Survey (ATLAS; Mao et al. 2012), the Mobile Astronomical Systems of the Telescope-Robots (MASTER; Lipunov 2003), Gaia (Altavilla et al. 2012), the Catalina Sky Survey (CSS; Christensen 2014), the Sloan Digital Sky Survey (SDSS; Frieman et al. 2008) and La Silla-QUEST Variability Survey (LSQ; Hadjiyska et al. 2012). (2) SNe discovered by quasi-untargeted searches that observe a large number of, almost randomly selected, galaxies. We deem the Lick Observatory Supernova Search (LOSS; Filippenko et al. 2001), the Lick Observatory and Tenagra Supernova Searches (LOTOSS), and the CHilean Automatic Supernova sEarch (CHASE; Pignata et al. 2009) as quasi-untargeted SN searches (consistent with Sanders et al. 2012). We include SNe discovered in the latter way in order to increase the sample size. 311 SNe are left after this selection.

Data availability Given that the wide field of view of the MUSE IFU spectrograph, the distant and low-mass galaxies with small angular diameters are less likely to be observed. Figure 2 shows the host

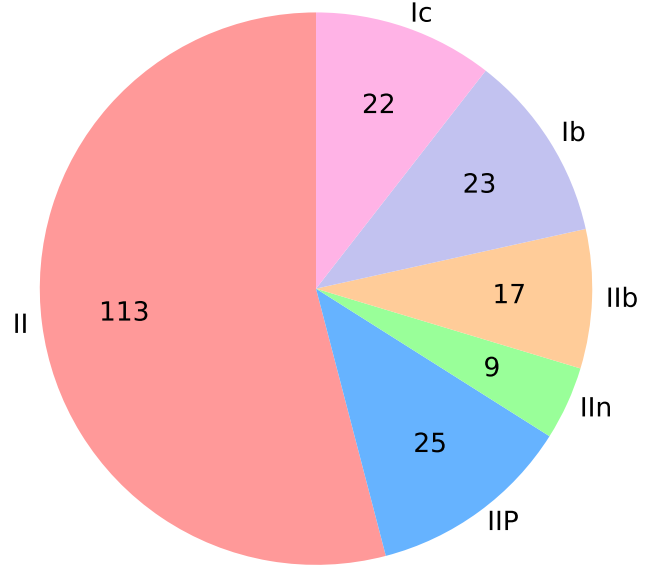


Figure 3. Number of SNe of different types in the final sample.

magnitude distribution for the above-selected SNe with MUSE data at different redshifts. For comparison, we use all SNe discovered after 2016 as an unbiased reference. It is clear that SNe with $0.02 < z < 0.05$ are systematically biased toward brighter host galaxies. On the other hand, SNe with $z \leq 0.02$ are similar to the reference sample. Therefore, we deem SNe with MUSE data at $z \leq 0.02$ to be an unbiased sample, which is representative of the SN population in the local Universe. In addition, there are circumstances where the host galaxies are observed by MUSE, but the SNe themselves are out of the field of view. We point out that such targets should be included, since they often reside in the low-metallicity outskirts of the host galaxies and excluding them would introduce significant biases. After this selection, 226 SNe remain in our sample.

There are 25 of Type IIP, 9 of Type IIn, 17 of Type IIb, 23 SNe of Type Ib, 22 of Type Ic. In addition, there are 113 Type II SNe in our sample, but their subtypes (IIP, IIL, IIb, IIn) are unknown; for simplicity, we shall refer to these sources simply as Type II throughout this paper. There are also 2 peculiar Type II, 3 peculiar Type Ib, 1 peculiar Type Ic, 1 Type Ibn, 1 Ca-rich Type Ib/Ic, 5 broad-lined Type Ic (Ic-BL), 1 Type Ib/c-BL, and 3 ambiguous Type IIn/LBV; these peculiar or ambiguous SNe are not included in our analysis, leaving 209 SNe in the final sample. Details of the final sample are provided in Table A1, and the distribution of SN types is shown in Figure 3.

2.2 Metallicity measurement

The reduced MUSE datacube were obtained from the ESO Data Archive. We used the IFUANA package (Lyman et al. 2018) to analyze the datacube. First we dereddened the datacube with Galactic extinction from Schlafly & Finkbeiner (2011), and a standard extinction law with $R_V = 3.1$ (Cardelli et al. 1989). We then applied redshift corrections to the datacube with redshifts from OSC and TNS. To acquire the spatially-resolved metallicity distribution across the galaxies, we employed the Voronoi binning with a target signal-to-noise ratio (SNR) of 120 within the wavelength range of 6540-6580

Å, within which the $H\alpha$ + [N II] lines reside. As will be described later, a minimum of 10 bins is required to fit the metallicity gradients; should fewer than 10 bins be found, we reduced the target SNR until 10 bins were achieved from the Voronoi binning. Due to differences in observation conditions and intrinsic galaxy properties, the number of bins for each galaxy varied from tens to several hundreds.

Inside each bin, we used `STARLIGHT` (Cid Fernandes et al. 2005) to fit and remove the stellar continuum, leaving only the nebular emission lines from ionized gas. Gaussian fitting is used to derive the fluxes of lines including $H\alpha$, $H\beta$, [O III] $\lambda\lambda$ 4959, 5007, and [N II] $\lambda\lambda$ 6548, 6583. We determined the gas-phase metallicity using the strong-line method based on the O3N2 calibration from Marino et al. (2013). This method uses the ratio of strong lines with similar wavelengths, making it insensitive to extinction.

$$12 + \log(O/H) = 8.533 - 0.214 \times O3N2, \quad (1)$$

where

$$O3N2 = \log \left(\frac{[O\ III]\lambda 5007}{H\beta} \times \frac{H\alpha}{[N\ II]\lambda 6583} \right) \quad (2)$$

For bins where [O III] or $H\beta$ were not detected (i.e., with amplitudes less than three times the spectral noise fluctuations), we used the N2 calibration instead

$$12 + \log(O/H) = 8.743 + 0.462 \times N2, \quad (3)$$

where

$$N2 = \log \left(\frac{[N\ II]\lambda 6583}{H\alpha} \right) \quad (4)$$

If the [N II] emission line was also too weak to be reliably detected, we tried to estimate an upper limit for the metallicity. Specifically, we derived the [N II] line width using the observed $H\alpha$ line width and the wavelength-dependent line spread function model of MUSE (Guérou et al. 2017). This width, combined with the 3σ amplitude limit, allowed us to estimate an upper limit of the [N II] line flux, and in turn, an upper limit of the metallicity.

The typical measurement uncertainty is 0.18 dex for the strong-line method (Marino et al. 2013). To reduce the metallicity uncertainties for the SNe, we used the galaxy metallicity gradient, calculated based on a large number of bins, to constrain the metallicity at the SN position. By using the spatial distribution characteristics of galaxy-wide metallicity, gradient fitting integrates information from multiple observation points, reduces the impact of local measurement uncertainties and enables safe extrapolation within a certain range. This effectively reduces the uncertainty in estimating metallicity at the SN position. For each Voronoi bin, we calculated the deprojected distances to the galaxy center using the inclination and position angles from HyperLEDA; for some host galaxies, this information is not available and we derived the inclination and position angles by manually fitting the images. We fit the metallicity gradient using Bayesian regression, assuming Gaussian uncertainties for the individual metallicity measurements. The derived gradient was then used to estimate the metallicity at the SN position. In some circumstances, the SNe reside outside of, but not too far away from, the distance range, so we could safely extrapolate the gradient to derive the metallicity. In addition, as discussed in the review by (Anderson et al. 2015), metallicity gradients are stronger in undisturbed galaxies and weaker in disturbed ones, while Sánchez-Blázquez et al. (2014) showed that some gradients invert in central regions. We observed similar phenomena in certain galaxies.

For some galaxies, it is difficult to fit a metallicity gradient, including the edge-on galaxies, for which we could not derive the

Table 1. Mean, median, and standard deviation values of $12+\log(O/H)$ for different SN types. The errors originate from measurement uncertainties.

SN Type	Mean [dex]	Median [dex]	Standard Deviation [dex]
II	8.45 ± 0.01	8.48 ± 0.01	0.15
IIP	8.39 ± 0.02	8.43 ± 0.02	0.16
IIn	8.47 ± 0.04	8.50 ± 0.05	0.17
I Ib	8.37 ± 0.03	8.37 ± 0.04	0.15
I b	8.46 ± 0.02	8.49 ± 0.02	0.13
I c	8.48 ± 0.02	8.52 ± 0.02	0.12

deprojected distances, and those galaxies with too few Voronoi bins. In such cases, we calculated the metallicity from a local bin centered on the SN with a radius of 300 pc or the seeing-limited spatial resolution, whichever is larger. For SN2016hbb, SN2018eog, and SN2018dfh, we had to use a local bin to measure their metallicity, but the SNe were still very bright during the observations; therefore, we could not get an accurate metallicity measurement because of the SN contamination. These three were excluded from our analysis.

3 RESULTS AND DISCUSSION

With the method described above, we derived the metallicity for all SNe in our sample (listed in Table A1). For example, Figure 4 displays the RGB composite images, H II regions, metallicity maps, and metallicity gradients of 4 host galaxies, with which we derived the metallicities for 7 SNe. Figure 5 shows the cumulative metallicity distributions for all SNe and for different Types. For SN2014cw and SN2016dsb, the [N II] lines are below the detection limit, allowing only upper limits to be determined; therefore, they are not included in Figure 5. The metallicities span a range from $12 + \log(O/H) = 8.1$ to 8.7 dex. Assuming Gaussian measurement errors, we employed a multiple resampling approach to calculate the mean, median and standard deviation values of the metallicity distributions (the results are listed in Table 1). The mean and median values are typically 8.4–8.5 dex, and the standard deviations are typically 0.12–0.16 dex. The differences among different SN types are very small. Type I Ib and Type I c have apparently the most different metallicity distributions, with mean (median) values of 8.37 (8.37) and 8.48 (8.52), respectively.

3.1 Is there any significant metallicity difference among SN types?

For the derived metallicity distributions, we carried out an experiment to study whether the apparent difference among SN types is real or due to the stochastic sampling effect. We used the metallicity distribution of all SNe, regardless of types, as a reference distribution. We then randomly drew $N = 20$ SNe (i.e. the typical number of SNe for Types IIP, I Ib, I b, and I c in our sample) from the full sample and plotted their metallicity distribution. This process was repeated 10,000 times to show how the metallicity distributions vary due to the stochastic sampling effect. The results are shown in Figure 5. The stochastic sampling effect can cause a 1σ uncertainty of ~ 0.05 dex in the distributions. The metallicity distributions for different SN types are all consistent with the reference distribution within $1-2\sigma$ uncertainties. The only exception is for Type I Ib, which deviates from the reference distribution by more than 2σ but is still within 3σ uncertainties.

We also performed the above experiment by varying the number of

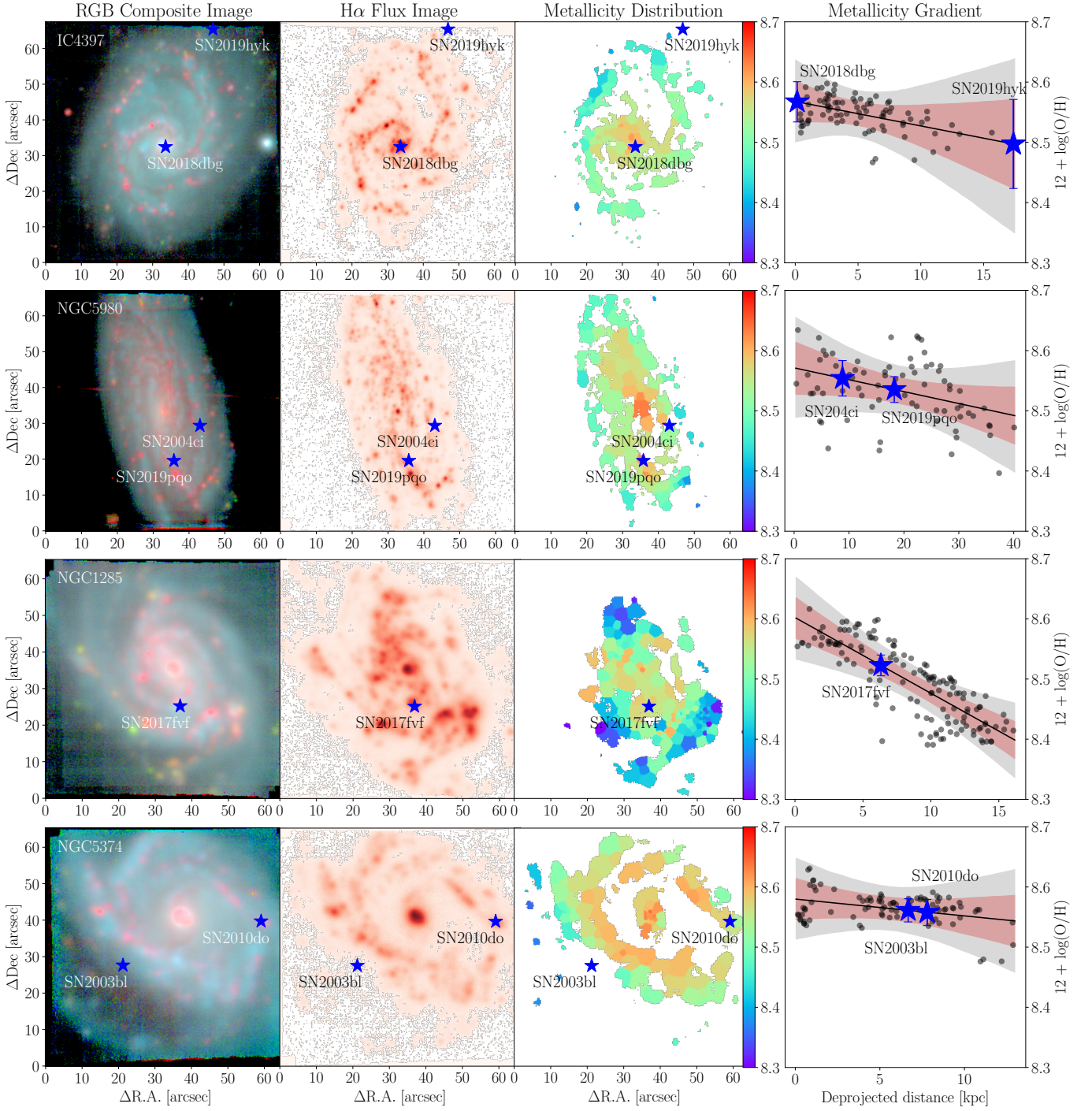


Figure 4. Example results of metallicity measurements for 7 SNe located in 4 host galaxies. Column 1: RGB images of host galaxies generated from MUSE datacube. The RGB components correspond to the cumulative fluxes from three spectral bands: 6550–6750 Å, 4950–5150 Å, and 4750–4950 Å respectively. Column 2: $H\alpha$ flux maps generated by simulating narrowband filter (6548–6578 Å) observations of the MUSE datacube. The continuum is fitted and subtracted using flux measurements from two adjacent wavelength bands: 6488–6518 Å on the blue side and 6608–6638 Å on the red side of the emission line. The color scale is in arbitrary units. Column 3: Metallicity distribution maps derived with the strong-line method. Column 4: Metallicity gradient fitting results. Black dots represent metallicity measurements for individual bins. The solid line shows the Bayesian regression fit for the metallicity gradient, while the red and gray shaded regions indicate the 1σ and 2σ confidence intervals, respectively. The blue stars mark the SN locations.

randomly chosen SNe. Figure 6 shows the probability distributions of the mean values of the resampled SN metallicities as a function of sample size. For the Types IIP, IIc, IIb, Ib and Ic, the typical uncertainty for their mean metallicities caused by stochastic sampling is ~ 0.05 dex, much larger than those propagated from metallicity mea-

surement errors (Table 1). The measured mean metallicities for different SN types are all consistent with that of the reference distribution within 3σ uncertainties. Therefore, the metallicity distributions of different SN types are not significantly different and are all consistent with being randomly drawn from the same reference distribution.

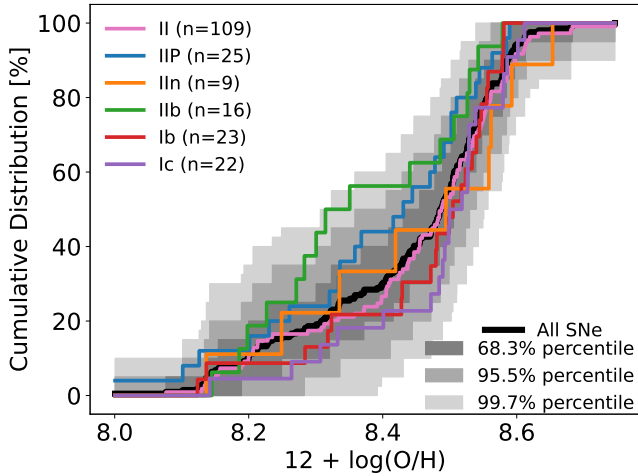


Figure 5. Cumulative metallicity distributions for different types of CCSNe. The black line represents the metallicity distribution for all SNe in the sample. The grey-shaded regions (from dark to light) indicate the 1σ , 2σ , and 3σ uncertainties caused by the stochastic sampling effect for a $N = 20$ subsample as estimated from our random resampling experiment.

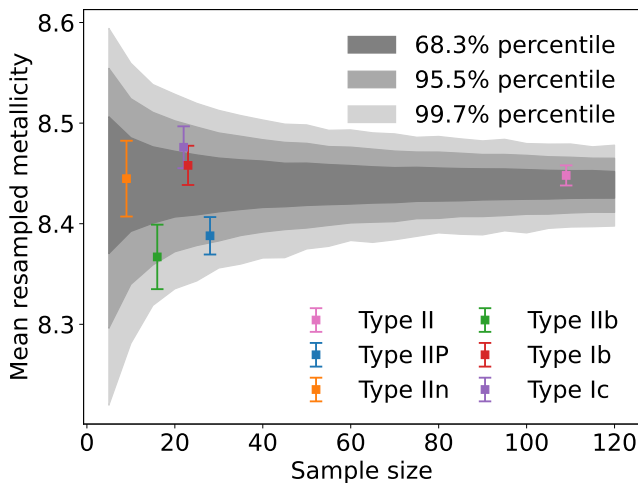


Figure 6. Data points: the number and mean metallicities for different types of CCSNe; the error bars are propagated from individual metallicity measurement uncertainties. Shaded regions: the 1σ , 2σ and 3σ (from dark to light) distributions of the mean values of randomly resampled SN metallicities from the full sample.

As an alternative method, we carried out a Kolmogorov-Smirnov (KS) test and calculated a p -value for each pair of SN types. In the KS test, the p -value assesses the degree of agreement between two sample distributions. Typically, a p -value less than 0.05 indicates a statistically significant difference between the two samples; conversely, a p -value greater than 0.05 indicates insufficient evidence to reject the null hypothesis that the two samples are drawn from the same distribution. The results are shown in Figure 7. The p -values are generally very large, suggesting very weak metallicity differences among SN types. Even for the apparently most distinct Type IIb and Type Ic, the p -value is ~ 0.1 and not small enough to indicate a significant metallicity difference between the two types.

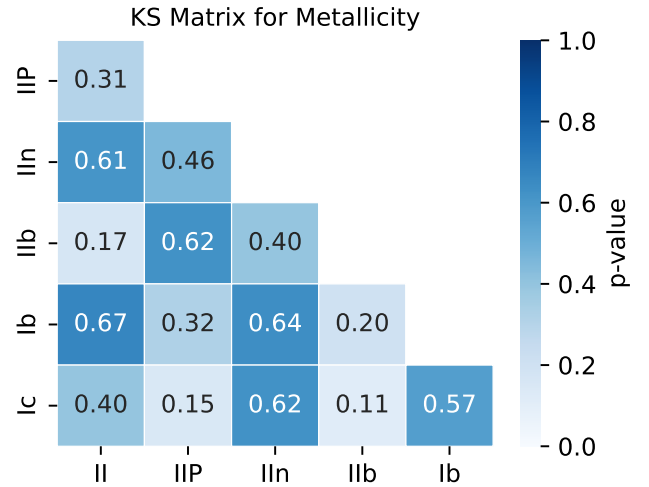


Figure 7. The p -value from KS test for each pair of SN types.

3.2 Comparison with previous results

Sanders et al. (2012) studied the environments of a sample of SNe discovered by untargeted SN searches. They observed 75 Types IIb, Ib, Ic and Ic-BL SNe using the 6.5 m Magellan Telescopes at Las Campanas Observatory in Chile. They claimed a marginally significant difference between Type Ib and Type Ic SNe (with a p -value of ~ 0.1 from KS test) and suggested that this difference may influence $\lesssim 30\%$ of stellar winds. This study relied on long-slit spectroscopy, however and was unable to spatially resolve the host galaxies.

Kuncarayakti et al. (2012a,b, 2013a,b, 2015, 2018) pioneered in using IFU spectroscopy to study SN environments. They investigated ~ 100 SNe of different types based on observations with VLT (MUSE, VIMOS and SINFONI), Gemini-North (GMOS) and the Hawaii 2.2-m telescope (SNIFS). They found no significant metallicity differences among SN types (Kuncarayakti et al. 2018). By the time of their studies, however, most SNe were discovered by targeted searches and it is unclear whether this potential bias may influence their sample.

Galbany et al. (2016, 2018) compiled a large collection of SN host galaxies (i.e. the PISCO sample) based on IFU observations with the 3.5-m CAHA telescope at the Calar Alto Observatory in Spain. Their sample contained 272 SNe (including 120 Type Ia SNe and 152 CCSNe) in 232 host galaxies. As noticed by themselves, most SNe in their sample were from targeted searches, therefore introducing a bias in the derived metallicity distributions. They also constructed an unbiased sample from archival data and found that Type II and Type Ic SNe display the highest metallicities while Type IIb and Type Ib SNe have lower metallicities. However, their KS test shows that this difference is not very significant.

Pessi et al. (2023) conducted IFU observations with VLT/MUSE of an unbiased sample of CCSNe discovered by the ASAS-SN survey (i.e. the AMUSING program). Their sample included a total of 112 CCSNe and they did not find any significant metallicity differences among the SN types. However, most SNe in their sample are of Type II and very few are of the other types (9 IIIn, 7 IIb, 7 Ib, 4 Ic, 3 IIIn, 2 Ic-BL). So their result may suffer more from the stochastic sampling effect.

In summary, the previous studies have not found any significant metallicity differences among the main CCSN types (II, IIP, IIIn, IIb, Ib and Ic). Now based on a larger and unbiased sample with

IFU observations, our study further confirms this conclusion. The typical uncertainty caused by stochastic sampling is narrowed down to ~ 0.05 dex and our careful analysis shows that all the SN types are consistent within a 3σ level.

3.3 The role of metallicity in SN progenitors

In the single-star progenitor channel, SESNe originate from massive WR stars, whose outer envelopes are stripped by their stellar winds (Conti 1978). The strength of line-driven wind is very sensitive to metallicity (Castor et al. 1975; Kudritzki & Puls 2000; Vink et al. 2001) and one may expect an increasing trend in metallicity for Types IIP, IIb, Ib and Ic with increasing degrees of envelope stripping. However, our result shows no significant metallicity difference between these SN types. It is possible that the binary progenitor channel dominates the origin of most SESNe. In this case, the dependence on metallicity is minimal, while binary parameters (such as orbital separation and secondary-to-primary mass ratio) exert a greater influence. This conclusion is consistent with those based on SN fraction (Smith et al. 2011), direct progenitor/companion detections (Crockett et al. 2008; Folatelli et al. 2015; Niu et al. 2024b; Sun et al. 2020a,b, 2021, 2022), nebular spectroscopy (Maeda et al. 2006, 2014, 2015; Fang & Maeda 2018), and light curve modeling (Lyman et al. 2016; Taddia et al. 2018; Woosley et al. 2021).

Recent studies suggest that Roche-lobe stripping may become significantly less efficient at low metallicities (Götberg et al. 2017). In high-metallicity stars, the greater opacity in the outer layers can trap radiation and the higher radiative pressure can help to expel the hydrogen envelope. In low-metallicity stars, however, the lower opacity allows radiation to escape more easily, thus reducing the radiative pressure and keeping the hydrogen envelope cooler and more tightly bound; therefore, it is easier for a low-metallicity mass donor to retain a significant hydrogen envelope after binary interaction, and this will result in a Type IIb, instead of a Type Ib, SN explosion. In our result, Type IIb SNe seem to have the lowest metallicities, but this difference is not significant enough to support this hypothesis. Future studies with even larger samples will be necessary to reveal the possible metallicity differences among SN types.

4 SUMMARY AND CONCLUSIONS

In this work, we studied the metallicity of CCSNe based on a large and unbiased sample with IFU observations. We carefully selected nearby CCSNe with archival VLT/MUSE data by considering the potential biases introduced by SN discovery and data availability. The final sample contains 209 CCSNe at a redshift of $z \leq 0.02$ discovered by (quasi-) untargeted SN searches, covering the main CCSN types of II (with unknown subtypes), IIP, IIb, Ib and Ic. Such a sample is representative of the SN population in the local Universe and is to date the largest sample for SN metallicity studies based on IFU observations.

For each SN host galaxy, we derived the spatially-resolved metallicity map with the strong-line method and estimated the SN metallicity with the galaxy metallicity gradient. The derived metallicities range from $12 + \log(\text{O}/\text{H}) = 8.1$ to 8.7 dex; for different SN types, the mean and median values are typically 8.4 – 8.5 dex, and the standard deviations are typically 0.12 – 0.16 dex.

With a random resampling experiment and a KS test, we show that there is no significant metallicity difference among the analyzed SN types. They can all be considered as being drawn randomly from the same reference distribution. With our large sample, the

uncertainty caused by the stochastic sampling effect is narrowed down to ~ 0.05 dex, and the metallicity distributions of different SN types are all consistent within 3σ uncertainties.

In the single-star progenitor channel, where mass loss is dominated by metallicity-dependent line-driven wind, we expect an increasing trend of metallicity for IIP \rightarrow IIb \rightarrow Ib \rightarrow Ic with increasing degrees of envelope stripping. However, our result suggests that metallicity plays a very minor role in the origin of SESNe. It is possible that most SESNe are from the binary progenitor channel, where the final fate of massive stars is insensitive to metallicity but is primarily determined by the binary parameters (e.g. secondary-to-primary mass ratio, binary separation).

Some theoretical studies suggest that Roche-lobe stripping becomes less efficient at low metallicities such that the progenitor may retain a significant hydrogen envelope and result in a Type IIb SN explosion. In our results, although the metallicities of Type IIb SNe are lower by more than 2σ uncertainties, they are still consistent with the reference distribution within 3σ uncertainties. Future studies with even larger samples will be necessary to reveal the possible metallicity differences among SN types.

ACKNOWLEDGMENTS

This work is supported by the Strategic Priority Research Program of the Chinese Academy of Sciences, Grant No. XDB0550300. NCS's research is funded by the NSFC grants No. 12303051 and No. 12261141690 and ZNX acknowledges support from the NSFC through grant No. 12303039. JFL acknowledges support from the NSFC through grants No. 11988101 and No. 11933004 and from the New Cornerstone Science Foundation through the New Cornerstone Investigator Program and the XPLORER PRIZE.

DATA AVAILABILITY

All data are publicly available from the ESO Data Archive :<https://archive.eso.org/scienceportal/home>.

REFERENCES

- Altavilla G., Botticella M. T., Cappellaro E., Turatto M., 2012, *Ap&SS*, **341**, 163
- Anderson J. P., Covarrubias R. A., James P. A., Hamuy M., Haberman S. M., 2010, *MNRAS*, **407**, 2660
- Anderson J. P., James P. A., Haberman S. M., Galbany L., Kuncarayakti H., 2015, *Publ. Astron. Soc. Australia*, **32**, e019
- Arnett W. D., Bahcall J. N., Kirshner R. P., Woosley S. E., 1989, *ARA&A*, **27**, 629
- Bacon R., et al., 2010, in McLean I. S., Ramsay S. K., Takami H., eds, Society of Photo-Optical Instrumentation Engineers (SPIE) Conference Series Vol. 7735, Ground-based and Airborne Instrumentation for Astronomy III. p. 773508 ([arXiv:2211.16795](https://arxiv.org/abs/2211.16795)), doi:10.1117/12.856027
- Beasor E. R., Smith N., Jencson J. E., 2024, *arXiv e-prints*, p. [arXiv:2410.14027](https://arxiv.org/abs/2410.14027)
- Bellm E. C., et al., 2019, *PASP*, **131**, 018002
- Bethe H. A., Brown G. E., Applegate J., Lattimer J. M., 1979, *Nuclear Phys. A*, **324**, 487
- Bostroem K. A., et al., 2023, *ApJ*, **953**, L18
- Cao Y., Nugent P. E., Kasliwal M. M., 2016, *PASP*, **128**, 114502
- Cardelli J. A., Clayton G. C., Mathis J. S., 1989, *ApJ*, **345**, 245
- Castor J. I., Abbott D. C., Klein R. I., 1975, *ApJ*, **195**, 157
- Chambers K. C., et al., 2019, The Pan-STARRS1 Surveys ([arXiv:1612.05560](https://arxiv.org/abs/1612.05560)), <https://arxiv.org/abs/1612.05560>

- Christensen E., 2014, in Wozniak P. R., Graham M. J., Mahabal A. A., Seaman R., eds, *The Third Hot-wiring the Transient Universe Workshop*. pp 55–55
- Cid Fernandes R., Mateus A., Sodré L., Stasińska G., Gomes J. M., 2005, *MNRAS*, **358**, 363
- Conti P. S., 1978, *ARA&A*, **16**, 371
- Crockett R. M., et al., 2008, *MNRAS*, **391**, L5
- Dályá G., et al., 2018, *MNRAS*, **479**, 2374
- Edmunds M. G., Pagel B. E. J., 1984, *MNRAS*, **211**, 507
- Fang Q., Maeda K., 2018, *ApJ*, **864**, 47
- Filippenko A. V., 1997, *ARA&A*, **35**, 309
- Filippenko A. V., Li W. D., Treffers R. R., Modjaz M., 2001, in Paczynski B., Chen W.-P., Lemme C., eds, *Astronomical Society of the Pacific Conference Series Vol. 246, IAU Colloq. 183: Small Telescope Astronomy on Global Scales*. p. 121
- Folatelli G., Bersten M. C., Kuncarayakti H., Benvenuto O. G., Maeda K., Nomoto K., 2015, *ApJ*, **811**, 147
- Frieman J. A., et al., 2008, *AJ*, **135**, 338
- Galbany L., Stanishev V., Mourão A., 2014, in Ray A., McCray R. A., eds, *IAU Symposium Vol. 296, Supernova Environmental Impacts*. pp 350–351, doi:10.1017/S1743921313009770
- Galbany L., et al., 2016, *A&A*, **591**, A48
- Galbany L., et al., 2018, *ApJ*, **855**, 107
- Götberg Y., de Mink S. E., Groh J. H., 2017, *A&A*, **608**, A11
- Guérou A., et al., 2017, *A&A*, **608**, A5
- Guillochon J., Parrent J., Kelley L. Z., Margutti R., 2017, *ApJ*, **835**, 64
- Hadjijska E., et al., 2012, in Griffin E., Hanisch R., Seaman R., eds, *IAU Symposium Vol. 285, New Horizons in Time Domain Astronomy*. pp 324–326 (arXiv:1210.1584), doi:10.1017/S1743921312000944
- Hong X., Sun N.-C., Niu Z., Wu J., Xi Q., Liu J., 2024, arXiv e-prints, p. arXiv:2411.14685
- Kiewe M., et al., 2012, *ApJ*, **744**, 10
- Kochanek C. S., 2014, *ApJ*, **785**, 28
- Kochanek C. S., et al., 2017, *PASP*, **129**, I04502
- Kudritzki R.-P., Puls J., 2000, *ARA&A*, **38**, 613
- Kuncarayakti H., et al., 2012a, in Roming P., Kawai N., Pian E., eds, *IAU Symposium Vol. 279, Death of Massive Stars: Supernovae and Gamma-Ray Bursts*. pp 343–344, doi:10.1017/S1743921312013269
- Kuncarayakti H., et al., 2012b, in Aoki W., Ishigaki M., Suda T., Tsujimoto T., Arimoto N., eds, *Astronomical Society of the Pacific Conference Series Vol. 458, Galactic Archaeology: Near-Field Cosmology and the Formation of the Milky Way*. p. 43
- Kuncarayakti H., et al., 2013a, *AJ*, **146**, 30
- Kuncarayakti H., et al., 2013b, *AJ*, **146**, 31
- Kuncarayakti H., et al., 2015, *Publication of Korean Astronomical Society*, **30**, 139
- Kuncarayakti H., et al., 2018, *A&A*, **613**, A35
- Langer N., Norman C. A., 2006, *ApJ*, **638**, L63
- Law N. M., et al., 2009, *PASP*, **121**, 1395
- Leloudas G., et al., 2011, *A&A*, **530**, A95
- Lipunov V. M., 2003, in *American Astronomical Society Meeting Abstracts #202*. p. 47.02
- Lunnan R., et al., 2014, *ApJ*, **787**, 138
- Lyman J. D., Bersier D., James P. A., Mazzali P. A., Eldridge J. J., Fraser M., Pian E., 2016, *MNRAS*, **457**, 328
- Lyman J. D., et al., 2018, *MNRAS*, **473**, 1359
- Maeda K., Nomoto K., Mazzali P. A., Deng J., 2006, *ApJ*, **640**, 854
- Maeda K., Katsuda S., Bamba A., Terada Y., Fukazawa Y., 2014, *ApJ*, **785**, 95
- Maeda K., et al., 2015, *ApJ*, **807**, 35
- Mao M. Y., et al., 2012, *MNRAS*, **426**, 3334
- Marino R. A., et al., 2013, *A&A*, **559**, A114
- Modjaz M., Kewley L., Bloom J. S., Filippenko A. V., Perley D., Silverman J. M., 2011, *ApJ*, **731**, L4
- Moriya T. J., et al., 2023, *A&A*, **677**, A20
- Neill J. D., et al., 2011, *ApJ*, **727**, 15
- Niino Y., Nagamine K., Zhang B., 2015, *MNRAS*, **449**, 2706
- Niu Z., Sun N.-C., Maund J. R., Zhang Y., Zhao R., Liu J., 2023, *ApJ*, **955**, L15
- Niu Z., Sun N.-C., Liu J., 2024a, *ApJ*, **966**, L20
- Niu Z., Sun N.-C., Liu J., 2024b, *ApJ*, **970**, L9
- Nomoto K., Suzuki T., Shigeyama T., Kumagai S., Yamaoka H., Saio H., 1993, *Nature*, **364**, 507
- Pagel B. E. J., Edmunds M. G., Blackwell D. E., Chun M. S., Smith G., 1979, *MNRAS*, **189**, 95
- Pessi T., et al., 2023, *A&A*, **677**, A28
- Pignata G., et al., 2009, in Giobbi G., Tornambe A., Raimondo G., Limongi M., Antonelli L. A., Menci N., Brocato E., eds, *American Institute of Physics Conference Series Vol. 1111, Probing Stellar Populations Out to the Distant Universe: Cefalu 2008, Proceedings of the International Conference*. AIP, pp 551–554 (arXiv:0812.4923), doi:10.1063/1.3141608
- Podsiadlowski P., Joss P. C., Hsu J. J. L., 1992, *ApJ*, **391**, 246
- Prieto J. L., Stanek K. Z., Beacom J. F., 2008, *ApJ*, **673**, 999
- Sánchez-Blázquez P., et al., 2014, *A&A*, **570**, A6
- Sanders N. E., et al., 2012, *ApJ*, **758**, 132
- Schlafly E. F., Finkbeiner D. P., 2011, *ApJ*, **737**, 103
- Smartt S. J., 2009, *ARA&A*, **47**, 63
- Smith N., 2014, *ARA&A*, **52**, 487
- Smith N., Li W., Filippenko A. V., Chornock R., 2011, *MNRAS*, **412**, 1522
- Sun N.-C., Maund J. R., Hirai R., Crowther P. A., Podsiadlowski P., 2020a, *MNRAS*, **491**, 6000
- Sun N.-C., Maund J. R., Crowther P. A., 2020b, *MNRAS*, **497**, 5118
- Sun N.-C., Maund J. R., Crowther P. A., Fang X., Zapartas E., 2021, *MNRAS*, **504**, 2253
- Sun N.-C., Maund J. R., Crowther P. A., Hirai R., Kashapov A., Liu J.-F., Liu L.-D., Zapartas E., 2022, *MNRAS*, **510**, 3701
- Sun N.-C., Maund J. R., Crowther P. A., 2023, *MNRAS*, **521**, 2860
- Taddia F., et al., 2015, *A&A*, **580**, A131
- Taddia F., et al., 2018, *A&A*, **609**, A136
- Tremonti C. A., et al., 2004, *ApJ*, **613**, 898
- Vink J. S., de Koter A., Lamers H. J. G. L. M., 2001, *A&A*, **369**, 574
- Woosley S. E., Weaver T. A., 1986, *ARA&A*, **24**, 205
- Woosley S. E., Sukhbold T., Kasen D. N., 2021, *ApJ*, **913**, 145
- Zapartas E., de Mink S. E., Justham S., Smith N., Renzo M., de Koter A., 2021, *A&A*, **645**, A6
- Zhao Y.-H., et al., 2024, arXiv e-prints, p. arXiv:2411.17969

APPENDIX A: SN DATA WITH METALLICITY

Table A1: SN Data with Metallicity. PA: Position angle of host galaxy; i : Inclination angle of host galaxy. $12+\log(\text{O}/\text{H})$: Oxygen abundance at SN location.

Name	Type	Host galaxy	Redshift	PA [deg]	i [deg]	$12+\log(\text{O}/\text{H})$ [dex]
PTF09gpn	II	Anonymous	0.0150	–	–	8.32 (+0.18/–0.18)
ASASSN-14dq	II	UGC 11860	0.0104	133.0	74.7	8.21 (+0.08/–0.08)
ASASSN-14dl	II	ESO 506-G4	0.0134	88.4	67.2	8.55 (+0.05/–0.05)
ASASSN-14dp	II	ESO 319-G15	0.0092	81.5	54.2	8.15 (+0.09/–0.09)
ASASSN-14ha	II	NGC 1566	0.0050	44.2	49.1	8.58 (+0.02/–0.02)
ASASSN-14ma	II	SDSS J235509.00+101252.9	0.0137	89.1	29.2	8.29 (+0.04/–0.04)
ASASSN-15fi	II	MRK 884	0.0172	45.5	40.0	8.13 (+0.01/–0.01)
ASASSN-15lx	II	ESO 47-G4	0.0126	90.5	48.7	8.21 (+0.05/–0.05)
ASASSN-15qh	II	ESO 534-G024	0.0102	112.0	55.6	8.41 (+0.09/–0.09)
PS15afa	II	NGC 3404	0.0150	81.3	86.7	8.60 (+0.14/–0.14)
ASASSN-15ln	II	UGC 546	0.0150	3.3	77.8	8.21 (+0.07/–0.07)
ASASSN-15fz	II	NGC 5227	0.0175	161.1	32.8	8.52 (+0.06/–0.06)
PS15aaa	II	IC 564	0.0190	68.2	77.3	8.51 (+0.06/–0.06)
ASASSN-15bb	II	ESO 381-IG48	0.0159	110.6	59.1	8.14 (+0.06/–0.06)
ASASSN-15jp	II	NGC 3157	0.0095	39.1	80.4	8.47 (+0.05/–0.05)
ASASSN-15oz	II	HIPASS J1919-33	0.0069	–	–	8.43 (+0.18/–0.18)
ASASSN-16ab	II	CGCG 012-116	0.0043	49.0	52.5	8.24 (+0.05/–0.05)
SMT16atf	II	PGC098793	0.0140	110.0	0.0	8.41 (+0.06/–0.06)
ASASSN-19kz	II	NGC 2207	0.0091	115.6	58.2	8.52 (+0.03/–0.03)
SN1998dl	II	NGC 1084	0.0044	39.9	49.9	8.46 (+0.01/–0.01)
SN1999dh	II	IC 211	0.0110	56.0	64.7	8.40 (+0.02/–0.02)
SN2001J	II	UGC 4729	0.0130	85.0	35.2	8.36 (+0.05/–0.05)
SN2003ao	II	NGC 2993	0.0081	93.7	35.8	8.44 (+0.01/–0.01)
SN2003E	II	ESO 485-G004	0.0149	142.9	90.0	8.31 (+0.18/–0.18)
SN2004ci	II	NGC 5980	0.0140	14.5	76.4	8.59 (+0.03/–0.03)
SN2004F	II	NGC 1285	0.0175	8.1	59.3	8.51 (+0.02/–0.02)
SN2005Z	II	NGC 3363	0.0190	179.2	45.3	8.62 (+0.06/–0.06)
SN2005H	II	NGC 838	0.0128	77.2	49.8	8.53 (+0.01/–0.01)
SN2006be	II	IC 4582	0.0071	172.1	83.1	8.37 (+0.14/–0.14)
SN2006cx	II	NGC 7316	0.0185	66.0	32.9	8.52 (+0.02/–0.02)
SN2006ca	II	UGC 11214	0.0088	175.0	16.5	8.41 (+0.06/–0.06)
SN2007rw	II	UGC 7798	0.0086	57.2	56.0	8.31 (+0.06/–0.06)
SN2008aw	II	NGC 4939	0.0104	7.4	70.1	8.68 (+0.19/–0.19)
SN2008fq	II	NGC 6907	0.0106	57.7	37.5	8.58 (+0.01/–0.01)
SN2008V	II	NGC 1591	0.0137	29.4	56.8	8.55 (+0.04/–0.04)
SN2009K	II	NGC 1620	0.0117	22.9	81.2	8.61 (+0.11/–0.11)
SN2009au	II	ESO 443-G21	0.0094	159.6	79.0	8.46 (+0.02/–0.02)
SN2009H	II	NGC 1084	0.0047	39.9	49.9	8.46 (+0.01/–0.01)
SN2009dq	II	IC 2554	0.0046	4.1	70.8	8.58 (+0.01/–0.01)
SN2010cl	II	MCG -02-25-20	0.0091	126.2	85.5	8.56 (+0.11/–0.11)
SN2010F	II	NGC 3120	0.0093	6.2	47.5	8.51 (+0.07/–0.07)
SN2010K	II	A120246+0224	0.0200	–	–	8.13 (+0.18/–0.18)
SN2012ga	II	NGC 6976	0.0200	164.9	27.1	8.50 (+0.06/–0.06)
SN2012cc	II	NGC 4419	0.0009	132.7	84.7	8.59 (+0.06/–0.06)
SN2013ej	II	NGC 628	0.0022	25.0	19.8	8.51 (+0.04/–0.04)
SN2014cw	II	PGC 68414	0.0060	–	–	< 8.28
SN2014cy	II	NGC 7742	0.0055	165.0	16.8	8.55 (+0.01/–0.01)
SN2014dw	II	NGC 3568	0.0082	7.0	67.0	8.48 (+0.02/–0.02)
SN2014V	II	NGC 3905	0.0193	62.5	48.7	8.53 (+0.04/–0.04)
SN2014ay	II	UGC 11037	0.0104	52.2	90.0	8.49 (+0.18/–0.18)
SN2015ay	II	UGC 722	0.0140	136.9	90.0	8.20 (+0.18/–0.18)
SN2016aqf	II	NGC 2101	0.0040	94.0	69.1	8.23 (+0.06/–0.06)
SN2016hgm	II	NGC 493	0.0080	59.9	74.6	8.44 (+0.08/–0.08)
SN2016blz	II	SDSS J154029.29+005437.4	0.0110	0.8	44.6	8.19 (+0.06/–0.06)

Continued on next page

Table A1: SN Data with Metallicity (continued)

Name	Type	Host galaxy	Redshift	PA [deg]	<i>i</i> [deg]	12+log(O/H) [dex]
SN2016ase	II	ESO 504- G 009	0.0150	123.1	47.0	8.14 (+0.15/−0.16)
SN2016hmq	II	PGC146262	0.0174	28.5	73.5	8.48 (+0.07/−0.07)
SN2016zb	II	MCG -03-25-015	0.0140	120.2	18.6	8.19 (+0.25/−0.25)
SN2016iyz	II	IC 2151	0.0104	93.4	61.5	8.49 (+0.03/−0.03)
SN2016cyk	II	2MASX J13024397-2656276	0.0161	70.0	55.8	8.56 (+0.04/−0.04)
SN2016bev	II	ESO 560-G013	0.0110	138.8	90.0	8.37 (+0.18/−0.18)
SN2016adl	II	GALEXASC J115155.68-132459.3	0.0070	–	–	8.08 (+0.18/−0.18)
SN2016bsb	II	Anonymous	0.0200	–	–	8.21 (+0.18/−0.18)
SN2017ffq	II	2MASX J17401447-5825586	0.0127	1140.8	74.4	8.45 (+0.05/−0.05)
SN2017fqk	II	NGC 1137	0.0101	16.05	59.54	8.48 (+0.11/−0.11)
SN2017pn	II	PGC959170	0.0140	38.0	62.4	8.20 (+0.07/−0.07)
SN2017fbq	II	2MASX J19334551-6058022	0.0150	161.0	81.1	8.33 (+0.06/−0.06)
SN2017gmr	II	NGC0988	0.0050	119.6	69.1	8.49 (+0.03/−0.03)
SN2017fqo	II	NGC 716	0.0150	59.0	75.9	8.43 (+0.19/−0.19)
SN2017auf	II	MCG -02-13-038	0.0133	111.3	73.6	8.61 (+0.06/−0.06)
SN2017ggw	II	ESO-246-G-21	0.0180	140.7	52.4	8.51 (+0.05/−0.05)
SN2017h xv	II	ESO 466- G 004	0.0160	134.4	41.3	8.60 (+0.07/−0.07)
SN2017faa	II	IC 4224	0.0180	99.3	84.2	8.39 (+0.08/−0.08)
SN2017jmk	II	NGC7541	0.0095	101.6	74.8	8.48 (+0.02/−0.02)
SN2017fbu	II	IC 211	0.0109	56.0	64.7	8.40 (+0.02/−0.02)
SN2017ahn	II	NGC3318	0.0090	79.4	59.8	8.50 (+0.02/−0.02)
SN2017ahn	II	NGC3318	0.0090	79.4	59.8	8.46 (+0.06/−0.06)
SN2017grn	II	IC1498	0.0180	2.9	90.0	8.60 (+0.18/−0.18)
SN2018cuf	II	IC5092	0.0108	26.9	28.6	8.61 (+0.19/−0.19)
SN2018bl	II	ESO 18-G9	0.0180	50.0	34.3	8.54 (+0.06/−0.06)
SN2018cvn	II	ESO 476- G 016	0.0190	141.1	59.6	8.45 (+0.19/−0.20)
SN2018kcw	II	IC 5179	0.0120	60.6	62.2	8.55 (+0.01/−0.01)
SN2018evy	II	NGC 6627	0.0180	74.5	26.9	8.53 (+0.03/−0.03)
SN2018dfg	II	NGC5468	0.0095	109.2	21.1	8.56 (+0.04/−0.04)
SN2018lab	II	IC2163	0.0092	102.6	78.2	8.53 (+0.01/−0.01)
SN2018ivc	II	NGC1068	0.0038	72.7	34.7	8.48 (+0.00/−0.00)
AT2018bbl	II	NGC 7421	0.0060	80.6	36.2	8.59 (+0.07/−0.07)
SN2018hyw	II	UGC 4344	0.0168	89.4	27.7	8.42 (+0.07/−0.08)
SN2018fit	II	CGCG 431-062	0.0140	130.6	81.5	8.54 (+0.27/−0.27)
SN2018pq	II	IC 3896A	0.0060	105.0	48.4	8.53 (+0.16/−0.15)
SN2018ant	II	MCG -02-22-22	0.0197	70.0	90.0	8.68 (+0.18/−0.18)
SN2019ltw	II	CGCG 137-076	0.0160	59.0	25.4	8.44 (+0.05/−0.05)
SN2019hyk	II	IC 4397	0.0147	160.1	48.3	8.50 (+0.07/−0.07)
SN2019tua	II	UGC 11860	0.0104	133.0	74.7	8.16 (+0.07/−0.06)
SN2019dxd	II	NGC 3464	0.0125	110.8	50.8	8.54 (+0.05/−0.05)
SN2019xis	II	Anonymous	0.0050	–	–	8.15 (+0.18/−0.18)
SN2020aqe	II	NGC 3836	0.0123	137.7	39.8	8.41 (+0.02/−0.02)
SN2020aze	II	NGC3318	0.0090	79.4	59.8	8.55 (+0.05/−0.05)
SN2020jfo	II	M61	0.0050	162.0	18.1	8.58 (+0.05/−0.05)
SN2020llx	II	NGC 7140	0.0099	17.4	49.6	8.55 (+0.08/−0.08)
SN2021abkm	II	NGC 6627	0.0176	74.5	26.9	8.58 (+0.11/−0.11)
SN2021agdm	II	ESO 61-8	0.0114	106.8	78.0	8.45 (+0.12/−0.12)
SN2021zgm	II	UGC 11289	0.0133	1.0	53.7	8.61 (+0.18/−0.18)
SN2022wsp	II	NGC 7448	0.0073	170.5	70.1	8.41 (+0.01/−0.01)
SN2022aau	II	NGC1672	0.0044	154.9	28.9	8.55 (+0.00/−0.00)
SN2022acko	II	NGC1300	0.0053	104.6	61.8	8.63 (+0.10/−0.11)
SN2022mmr	II	IC 1498	0.0173	2.9	90.0	8.56 (+0.18/−0.18)
SN2023dpj	II	NGC 5135	0.0137	126.4	24.8	8.51 (+0.02/−0.02)
SN2023rve	II	NGC 1097	0.0040	133.9	54.8	8.75 (+0.26/−0.25)
SN2023ijd	II	NGC 4568	0.0074	28.6	67.5	8.51 (+0.02/−0.02)
SN2024jlf	II	NGC5690	0.0058	145.1	75.9	8.47 (+0.06/−0.06)

Continued on next page

Table A1: SN Data with Metallicity (continued)

Name	Type	Host galaxy	Redshift	PA [deg]	i [deg]	$12+\log(\text{O}/\text{H})$ [dex]
ASASSN-14iz	IIP	ESO 462-G9	0.0193	162.3	58.8	8.48 (+0.15/−0.15)
ASASSN-15kz	IIP	IC 4303	0.0080	70.7	59.1	8.23 (+0.04/−0.04)
ASASSN-15ng	IIP	ESO 221-G12	0.0098	164.3	90.0	8.34 (+0.18/−0.18)
ASASSN-16at	IIP	UGC 8041	0.0044	168.3	54.0	8.32 (+0.07/−0.07)
SN1999br	IIP	NGC 4900	0.0032	135.0	19.0	8.43 (+0.02/−0.02)
SN2003bl	IIP	NGC 5374	0.0146	45.0	36.9	8.54 (+0.02/−0.02)
SN2003hg	IIP	NGC 7771	0.0143	68.0	66.7	8.58 (+0.02/−0.02)
SN2003bn	IIP	2MASX J10023529-2110531	0.0128	98.0	74.6	8.36 (+0.06/−0.06)
SN2012bu	IIP	NGC 3449	0.0109	145.8	90.0	8.49 (+0.18/−0.18)
SN2015W	IIP	UGC 3617	0.0130	8.5	49.0	8.10 (+0.20/−0.20)
SN2016blb	IIP	2MASX J11372059-0454450	0.0180	168.0	67.5	8.33 (+0.06/−0.06)
SN2016hvu	IIP	NGC 7316	0.0185	66.0	32.9	8.44 (+0.02/−0.02)
SN2016cok	IIP	M66	0.0020	168.2	67.5	8.59 (+0.03/−0.03)
SN2016L	IIP	UGCA 397	0.0090	120.0	19.0	8.20 (+0.05/−0.05)
SN2016B	IIP	CGCG 012-116	0.0043	49.0	52.5	8.26 (+0.06/−0.06)
SN2016I	IIP	UGC 09450	0.0149	49.0	90.0	8.13 (+0.18/−0.18)
SN2017fvr	IIP	UGC 3165	0.0130	135.0	61.0	8.42 (+0.07/−0.07)
SN2017aym	IIP	NGC 5690	0.0058	145.1	75.9	8.51 (+0.05/−0.05)
SN2017ivu	IIP	NGC 5962	0.0065	106.3	51.4	8.00 (+0.71/−0.71)
SN2017fvf	IIP	NGC 1285	0.0170	8.1	59.3	8.50 (+0.02/−0.02)
SN2017fem	IIP	IC 4452	0.0140	77.8	20.6	8.50 (+0.03/−0.03)
SN2017gry	IIP	ESO 155-G36	0.0193	171.9	82.4	8.54 (+0.05/−0.05)
SN2017ejx	IIP	NGC 2993	0.0081	93.7	35.8	8.47 (+0.01/−0.01)
SN2018yo	IIP	UGC 7840	0.0130	73.4	57.6	8.37 (+0.09/−0.09)
SN2018cho	IIP	IC 4	0.0167	12.0	45.6	8.56 (+0.04/−0.04)
ASASSN-14fd	IIn	PGC 43070	0.0154	16.0	51.5	8.34 (+0.07/−0.07)
ASASSN-15hs	IIn	2MASX J15333488-7807258	0.0091	177.3	39.9	8.56 (+0.03/−0.03)
ASASSN-16jt	IIn	ESO 344-G021	0.0108	58.0	67.3	8.56 (+0.06/−0.16)
SN1997bs	IIn	NGC 3627	0.0019	168.2	67.5	8.59 (+0.04/−0.04)
SN2013fc	IIn	ESO 154-G10	0.0186	87.9	35.5	8.65 (+0.05/−0.05)
SN2015bf	IIn	NGC 7653	0.0142	172.5	31.0	8.49 (+0.12/−0.12)
SN2016aiy	IIn	ESO 323-G084	0.0100	7.0	77.7	8.24 (+0.21/−0.20)
SN2016eso	IIn	ESO 422- G 019	0.0170	148.9	62.5	8.26 (+0.50/−0.50)
SN2021aefts	IIn	NGC 3836	0.0123	137.7	39.8	8.42 (+0.01/−0.01)
ASASSN-14az	I Ib	PGC 1101367	0.0067	12.0	68.8	8.20 (+0.13/−0.13)
ASASSN-15tu	I Ib	2MASX J22340166-3223490	0.0126	65.0	38.6	8.35 (+0.06/−0.06)
PS15apj	I Ib	NGC 6641	0.0140	100.0	29.9	8.51 (+0.06/−0.06)
ASASSN-15bd	I Ib	SDSS J155438.39+163637.6	0.0079	89.1	90.0	8.19 (+0.18/−0.18)
SN2008aq	I Ib	MCG -02-33-20	0.0080	175.0	90.0	8.14 (+0.18/−0.18)
SN2014cl	I Ib	IC 217	0.0063	35.1	82.6	8.27 (+0.28/−0.28)
SN2015bi	I Ib	VV 839	0.0160	143.3	52.4	8.31 (+0.08/−0.08)
SN2016dsb	I Ib	GALEXASC J015900.57-322225.2	0.0161	–	–	< 8.15
SN2016gkg	I Ib	NGC 613	0.0049	122.2	35.7	8.53 (+0.18/−0.18)
SN2016iyc	I Ib	UGC 11924	0.0127	120.2	61.4	8.30 (+0.05/−0.05)
SN2017mw	I Ib	ESO 316-G7	0.0120	158.7	70.0	8.23 (+0.02/−0.02)
SN2018ddr	I Ib	UGC 8896	0.0146	69.2	83.7	8.44 (+0.09/−0.09)
SN2018gix	I Ib	NGC 865	0.0100	159.3	90.0	8.54 (+0.18/−0.18)
SN2019pqo	I Ib	NGC 5980	0.0141	14.5	76.4	8.58 (+0.02/−0.02)
SN2019bao	I Ib	UGC 5687	0.0119	111.4	80.0	8.28 (+0.15/−0.15)
SN2020fqv	I Ib	NGC 4568	0.0075	28.6	67.5	8.53 (+0.02/−0.02)
SN2021bxu	I Ib	ESO 478-G6	0.0178	101.8	57.7	8.49 (+0.03/−0.03)
MASTEROT J120451.50 +265946.6	I Ib	NGC 4080	0.0019	121.1	75.6	8.47 (+0.10/−0.10)
PTF09dfk	I Ib	Anonymous	0.0160	99.4	44.6	8.32 (+0.07/−0.07)
iPTF13bvn	I Ib	NGC 5806	0.0045	171.8	60.4	8.52 (+0.04/−0.03)

Continued on next page

Table A1: SN Data with Metallicity (continued)

Name	Type	Host galaxy	Redshift	PA [deg]	<i>i</i> [deg]	12+log(O/H) [dex]
ASASSN-15ta	Ib	GALEXASC J202933.17-615703.5	0.0150	83.5	48.9	8.22 (+0.11/−0.12)
PS15cer	Ib	NGC 7349	0.0150	165.2	76.3	8.43 (+0.07/−0.07)
Gaia15acs	Ib	PGC 65805	0.0200	62.8	90.0	8.52 (+0.18/−0.18)
ASASSN-16ff	Ib	ESO 218-G008	0.0087	28.4	90.0	8.14 (+0.18/−0.18)
SN2004cc	Ib	NGC 4568	0.0075	28.6	67.5	8.50 (+0.05/−0.05)
SN2004dk	Ib	NGC 6118	0.0052	58.1	68.7	8.56 (+0.02/−0.02)
SN2006lc	Ib	SDSS J24424.36-000943.4	0.0161	66.1	51.8	8.56 (+0.04/−0.04)
SN2009iu	Ib	NGC 7329	0.0108	107.3	42.7	8.58 (+0.12/−0.12)
SN2012au	Ib	NGC 4790	0.0045	87.0	58.8	8.48 (+0.01/−0.01)
SN2014ge	Ib	NGC 4080	0.0019	121.1	75.6	8.43 (+0.07/−0.07)
AT2015dd	Ib	NGC 5483	0.0060	18.9	26.3	8.48 (+0.02/−0.02)
SN2016ajo	Ib	UGC 11344	0.0160	162.8	64.9	8.32 (+0.04/−0.04)
SN2016cdd	Ib	ESO 218-G008	0.0087	28.4	90.0	8.12 (+0.18/−0.18)
SN2017ewx	Ib	NGC 5418	0.0160	45.4	68.5	8.50 (+0.06/−0.06)
SN2019ehk	Ib	NGC 4321	0.0043	153.0	24.0	8.58 (+0.03/−0.03)
SN2019yvr	Ib	NGC 4666	0.0050	40.6	69.6	8.58 (+0.01/−0.01)
SN2020hvp	Ib	NGC 6118	0.0052	58.1	68.7	8.55 (+0.08/−0.08)
SN2020admc	Ib	ESO 320-G31	0.0100	144.7	90.0	8.53 (+0.18/−0.18)
SN2021kos	Ib	IC 719	0.0061	52.4	90.0	8.54 (+0.18/−0.18)
SN2023crx	Ib	NGC1602	0.0120	22.9	81.2	8.54 (+0.07/−0.07)
ASASSN-15kj	Ic	ESO 297-G37	0.0185	63.4	90.0	8.47 (+0.18/−0.18)
ASASSN-21vr	Ic	NGC 3256	0.0094	87.2	48.2	8.53 (+0.00/−0.00)
SN2002J	Ic	NGC 3464	0.0125	110.8	50.8	8.52 (+0.06/−0.06)
SN2002ao	Ic	UGC 9299	0.0051	29.8	24.7	8.26 (+0.09/−0.08)
SN2005lr	Ic	ESO 492-G2	0.0086	153.6	48.8	8.49 (+0.10/−0.10)
SN2007rz	Ic	NGC 1590	0.0130	110.0	27.9	8.61 (+0.03/−0.03)
SN2009dt	Ic	IC 5169	0.0104	24.1	84.0	8.58 (+0.04/−0.04)
SN2010do	Ic	NGC 5374	0.0146	45.0	36.9	8.53 (+0.02/−0.02)
SN2011N	Ic	ESO 120-G16	0.0114	0.6	77.4	8.50 (+0.05/−0.05)
SN2011jm	Ic	NGC 4809	0.0031	65.0	90.0	8.14 (+0.18/−0.18)
SN2013dk	Ic	NGC 4038	0.0055	160.4	51.9	8.54 (+0.00/−0.00)
SN2014L	Ic	NGC 4254	0.0080	60.0	20.1	8.60 (+0.01/−0.01)
SN2014eh	Ic	NGC 6907	0.0106	57.7	37.5	8.50 (+0.05/−0.05)
SN2016iae	Ic	NGC 1532	0.0040	34.2	83.0	8.53 (+0.07/−0.07)
SN2017fwm	Ic	ESO 141-IG32	0.0160	178.8	41.9	8.53 (+0.06/−0.06)
SN2017rt	Ic	NGC 3836	0.0120	137.7	39.8	8.40 (+0.02/−0.02)
SN2019yz	Ic	UGC 9977	0.0064	79.5	90.0	8.33 (+0.18/−0.18)
SN2020oi	Ic	MESSIER 100	0.0052	153.0	24.0	8.59 (+0.01/−0.01)
SN2021aexi	Ic	NGC 7771	0.0140	68.0	66.7	8.58 (+0.04/−0.04)
SN2021ocs	Ic	NGC 7828	0.0191	136.7	90.0	8.49 (+0.18/−0.18)
SN2023cj	Ic	NGC5468	0.0095	109.2	21.1	8.31 (+0.05/−0.05)
SN2023bjj	Ic	ESO-163-G011	0.0090	3.3	70.9	8.48 (+0.18/−0.18)

This paper has been typeset from a \LaTeX file prepared by the author.